

# We are IntechOpen, the world's leading publisher of Open Access books Built by scientists, for scientists

**4,800**

Open access books available

**122,000**

International authors and editors

**135M**

Downloads

Our authors are among the

**154**

Countries delivered to

**TOP 1%**

most cited scientists

**12.2%**

Contributors from top 500 universities



**WEB OF SCIENCE™**

Selection of our books indexed in the Book Citation Index  
in Web of Science™ Core Collection (BKCI)

Interested in publishing with us?  
Contact [book.department@intechopen.com](mailto:book.department@intechopen.com)

Numbers displayed above are based on latest data collected.

For more information visit [www.intechopen.com](http://www.intechopen.com)



# Virtual Instrument for Online Electrical Capacitance Tomography

Zhaoyan Fan, Robert X. Gao\* and Jinjiang Wang  
 Department of Mechanical Engineering, University of Connecticut,  
 USA

## 1. Introduction

Electrical capacitance tomography (ECT) is a technique invented in the 1980's to determine material distribution in the interior of an enclosed environment by means of external capacitance measurements (Huang et al., 1989a, 1992b). In a typical ECT system, 8 to 16 electrodes (Yang, 2010) are symmetrically mounted inside or outside a cylindrical container, as illustrated in Figure 1. During the period of a scanning *frame*, an excitation signal is applied to one of the electrodes and the remaining electrodes are acting as detector electrodes. Subsequently, the voltage potential at each of the detector electrodes is measured, one at a time, by the measurement electronics to determine the inter-electrode capacitance. Changes in these measured capacitance values indicate the variation of material distribution within the container, e.g. air bubbles translating within an oil flow. An image of permittivity distribution directly representing the materials distribution can be retrieved from the capacitance data through a back-projection algorithm (Isaksen, 1996). While image resolution associated with the ECT technique is lower than other tomographic techniques such as CT or optical imaging, it is advantageous in terms of its non-intrusive nature, portability, robustness, and no exposure to radiation hazard.

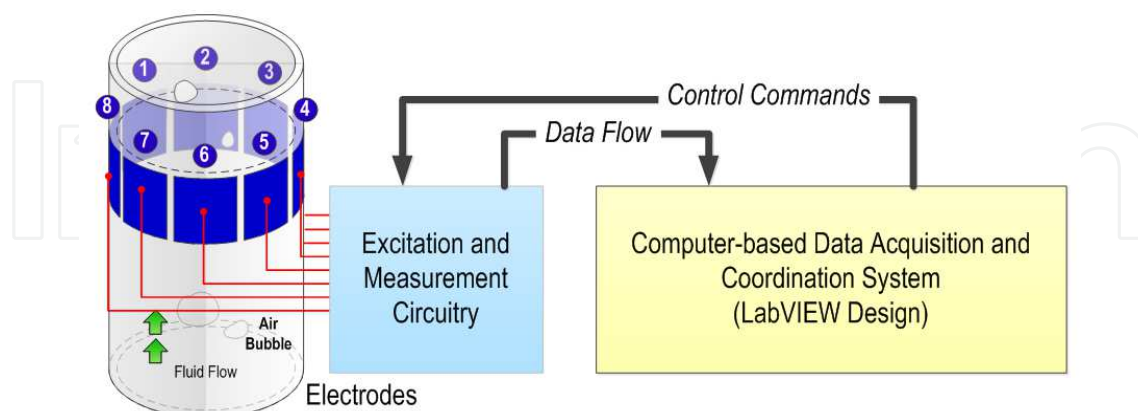


Fig. 1. Illustration of major components in an ECT system

As shown in Fig.1, an ECT system generally consists of three major components: 1) An excitation and measurement circuitry that drives the sensors and conditions the received signals; 2) A computer-based data acquisition (DAQ) and coordination system, to provide control logic for the sequential excitations of the electrodes and reconstruct tomographic

images of the materials; as well as 3) electrodes mounted on the outer (for non-metallic containers) or inner surface of the container.

According to the type of excitation signals being used, ECT can be divided into two categories: AC-based (sine-wave excitation) and charge-discharge-based (square-wave excitation). The former is advantageous in terms of measurement stability and accuracy, whereas the latter has lower circuit complexity (Huang et al., 1992). In recent years, studies have been conducted on sensing principle and circuit optimization to enhance the performances of ECT. For AC-based method, a multiple excitation scheme (Fan & Gao, 2011) has been designed and tested to increase the frame rate for higher time resolution in monitoring fast changing dynamics inside the container. The grouping method (Olmos et al., 2008) is another technique investigated to increase the magnitude of the received signals by combining two or more electrodes into one segment. ECT has also been applied to generate 3-D material distribution by mounting electrodes in multiple layers along the axis of the cylindrical container and detecting the cross-layer capacitance values (Marashdeh & Teixeira, 2004; Warsito et al., 2007). These efforts have expanded the scope of application of ECT, into such fields as measurement of multi-phase flows (gas-liquid and gas-solids, etc.) in pipelines, detection of leakage from buried water pipes, flow pattern identification (Reinecke & Mewes, 1996; Xie et al, 2006), etc. This chapter aims to introduce the realization of a computer-based DAQ and coordination system for ECT through Virtual Instrumentation (VI). Discussion will focus on the AC-based method, using single excitation and single detection channel, in which most of the basic functions required for various ECT techniques are included. The presentation provides design guidelines and recommendations for researchers to build ECT systems for specific applications.

## 2. VI design

According to the functions required for data acquisition, data processing, and circuit control, the VI is divided into seven major subVI's:

1. Switching control
2. Data sampling
3. Data calibration
4. Permittivity calculation
5. Mesh generation
6. Image generation
7. Image display

During a scanning frame, as shown in Figure 2, the **Switching Control** subVI divides the process into individual measurement steps according to the total number of capacitance values formed by all the electrodes. Connections of each electrode as well as the 8-1 multiplexer (MUX) in the measurement circuitry are controlled by the digital I/O (DIO) ports, such that the capacitance formed by each pair of electrodes is measured in each measurement step. After being processed by a pre-amplifier and lock-in amplifier, the voltage signal proportional to the capacitance value is sampled by the **Data Sampling** subVI. When all the capacitance values for a complete frame are sampled, they are normalized in the **Data Normalization** subVI and re-sorted into the form of matrix. The data is combined with the sensitivity matrix by the **Permittivity Calculation** subVI, and finally converted into an image representing the material permittivity distribution via the **Mesh Generation, Image Generation, and Image Display** subVI's. By looping the whole

process frame by frame, the VI controls the measurement circuit and samples the signal continuously to display the dynamics of the monitored process.

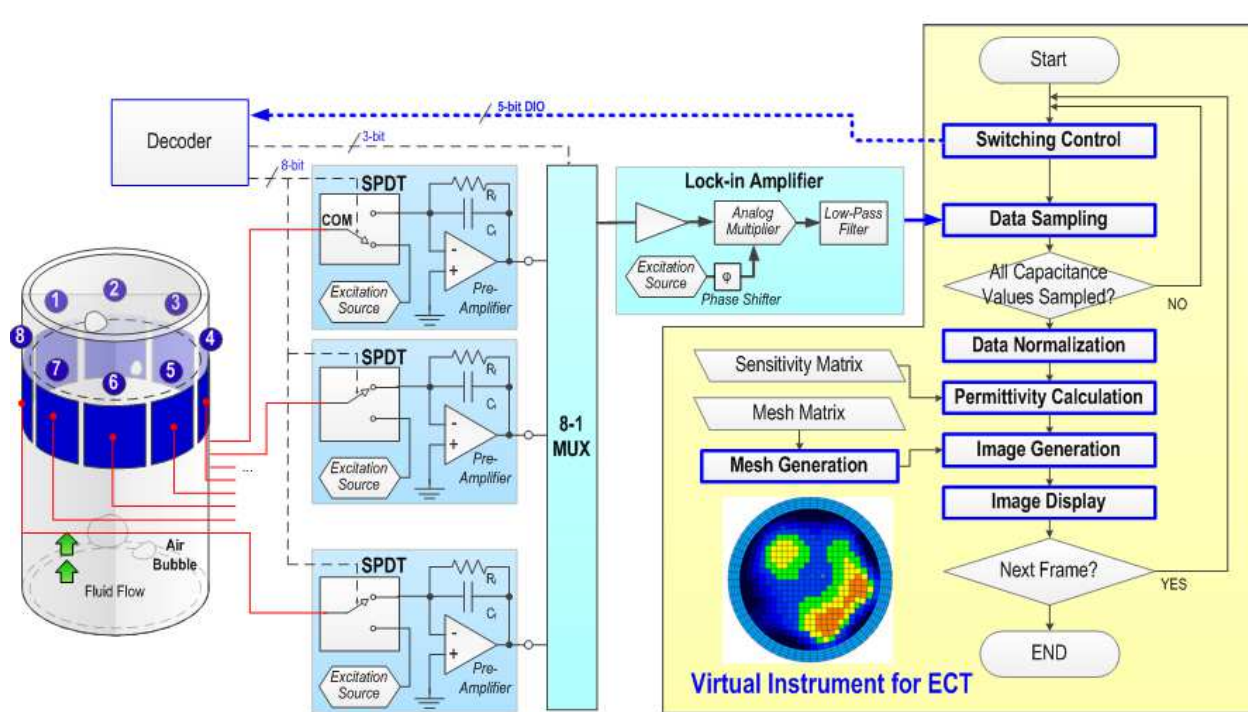


Fig. 2. A detailed view of an AC-based ECT system

## 2.1 Switching control

The basic procedure of AC-Based capacitance measurement is to apply a sinusoidal voltage signal to a pair of electrodes and measure the output current/voltage, from which the impedance or capacitance can be derived (Yang, 1996). Assuming there are  $N$  electrodes in the sensor being numbered from one to  $N$ , they are excited with the sinusoidal wave, one at a time. When one electrode is excited, other electrodes are kept at ground potential and act as detector electrodes. Physically, the function is realized by controlling the SPDT (Single-Pole-Double-Throw) switch and the analog MUX as shown in Figure 1. The common port of each SPDT switch is connected with one of the electrodes to enable switching between the non-inverting input of a pre-amplifier (detection mode) and the excitation source (excitation mode). In the detection mode, the output voltage amplitude of the pre-amplifier,  $V_{ij}$ , is a function of the measured inter-electrode capacitance (Huang et al., 1992), expressed as:

$$V_{ij} = -\frac{j2\pi f_e C_{ij} R_f}{j2\pi f_e C_f R_f + 1} V_e \quad (1)$$

where  $C_{ij}$  is the inter-electrode capacitance between electrodes  $i$  and  $j$  ( $1 \leq i, j \leq N$ ;  $i \neq j$ ).  $V_e$  and  $f_e$  are the voltage amplitude and frequency of the sine wave from the excitation source,  $R_f$  and  $C_f$  are the feedback resistance and capacitance of the pre-amplifier circuit. When the feedback resistance is chosen to satisfy the relationship  $|j2\pi f_e C_f R_f| \gg 1$ , e.g.  $f_e = 700$  kHz,  $C_f = 50$  pF, and  $R_f = 100$  M $\Omega$ , the voltage amplitude  $V_{ij}$  is approximately proportional to  $C_{ij}$ . The simplified relationship can be expressed as:

$$V_{ij} = -\frac{C_{ij}}{C_f} V_e \quad (2)$$

Through the lock-in amplifier, the output sine wave from pre-amplifier is mixed with the original excitation signal and then processed by a low pass filter. Thus a measurable DC voltage equal to the value of  $V_{ij}$  is available from the output of the lock-in amplifier during each individual measurement step.

The measurement protocol in the sensing electronics first measures the inter-electrode capacitance between electrodes one and two, then between one and three, and up to one and  $N$ . Then, the capacitances between electrodes two and three, and up to two and  $N$  are measured. For each scanning frame, the measurements continue until all the inter-electrode capacitances are measured and the capacitances can be represented in a matrix, which is symmetric with respect to the diagonal. Due to  $C_{ij} = C_{ji}$ , the minimum required capacitance can be expressed as (Alme & Mylvaganam, 2007):

$$\bar{C} = \begin{bmatrix} C_{12} & & & & \\ C_{13} & C_{23} & & & \\ \vdots & \vdots & & & \\ C_{1,N-1} & C_{2,N-1} & \dots & C_{N-2,N-1} & \\ C_{1,N} & C_{2,N} & \dots & C_{N-2,N} & C_{N-1,N} \end{bmatrix} \quad (3)$$

With  $N$  electrodes, this gives a total number of  $M$  independent capacitance measurements, where  $M$  can be expressed as (Williams & Beck, 1995):

$$M = \frac{N(N-1)}{2} \quad (4)$$

For an 8-electrode arrangement, Equation (4) gives 28 capacitance values or a total of 28 measurement steps required for each frame. Given that the SPDT switch and the 8-1 MUX is controlled by one ( $\log_2 2$ ) and three ( $\log_2 8$ ) digital ports, respectively, a total of  $8 \times 1 + 3 = 11$  digital ports are required to directly control the hardware. These digital ports can be either connected with the DIOS on the DAQ card directly, or through a decoder to reduce the control complexity as shown in Figure 2. The decoder translates the 5-bit digital number sent from the DIO into the 11-bit control codes to control the switches and MUX. Thus, the **Switching Control** subVI determines electrodes for excitation and detection in each step by sending a sequence number from 1 to 28 to the hardware decoder. Each of the sequence number corresponds to a specific inter-electrode configuration  $C_{ij}$ , as shown in Table 1.

Case #	0	1	2	3	...	5	6	...	9	10	...	14	15	...	20	21	...	27
$C_{ij}$	$C_{12}$	$C_{13}$	$C_{23}$	$C_{14}$	...	$C_{34}$	$C_{15}$	...	$C_{45}$	$C_{16}$	...	$C_{56}$	$C_{17}$	...	$C_{67}$	$C_{18}$	...	$C_{78}$
DT	1	1	2	1	...	3	1	...	4	1	...	5	1	...	6	1	...	7
EX	2	3	3	4	...	4	5	...	5	6	...	6	7	...	7	8	...	8

Table 1. Sequence of the inter-electrode capacitance measurement during a frame (EX: excitation electrode, DT: detection electrode)

Figure 3 shows the design of the **Switching Control** subVI. A *case structure* was created to generate the 28 sequence numbers in a binary form from 0x0001 (decimal 1, in case #0) to 1x1100 (decimal 28, in case #27). Within a **timed loop** structure, the loop counter  $i$  is used as a *measurement step indicator* to successively increase the control bit of the *case structure* till all the 28 capacitance values are measured. The time period of each measurement step is controlled by the loop timer,  $dt$ , with a unit of millisecond as shown in Figure 3. The value of  $dt$  finally determines the time resolution or the frame rate of ECT imaging. For example, when the value of  $dt$  is set to 4 [ms], the total time period for a frame is  $28 \times 4 = 112$  ms, corresponding to a maximum frame rate of 8.9 frames per second. The minimum resolution of timer setting is constrained to one millisecond in the general LabVIEW system. Such a limitation is shortened to microsecond level by applying the LabVIEW Real-Time module, to further increase the frame rate of ECT at the cost of DAQ hardware upgrading (National Instruments, 2001).

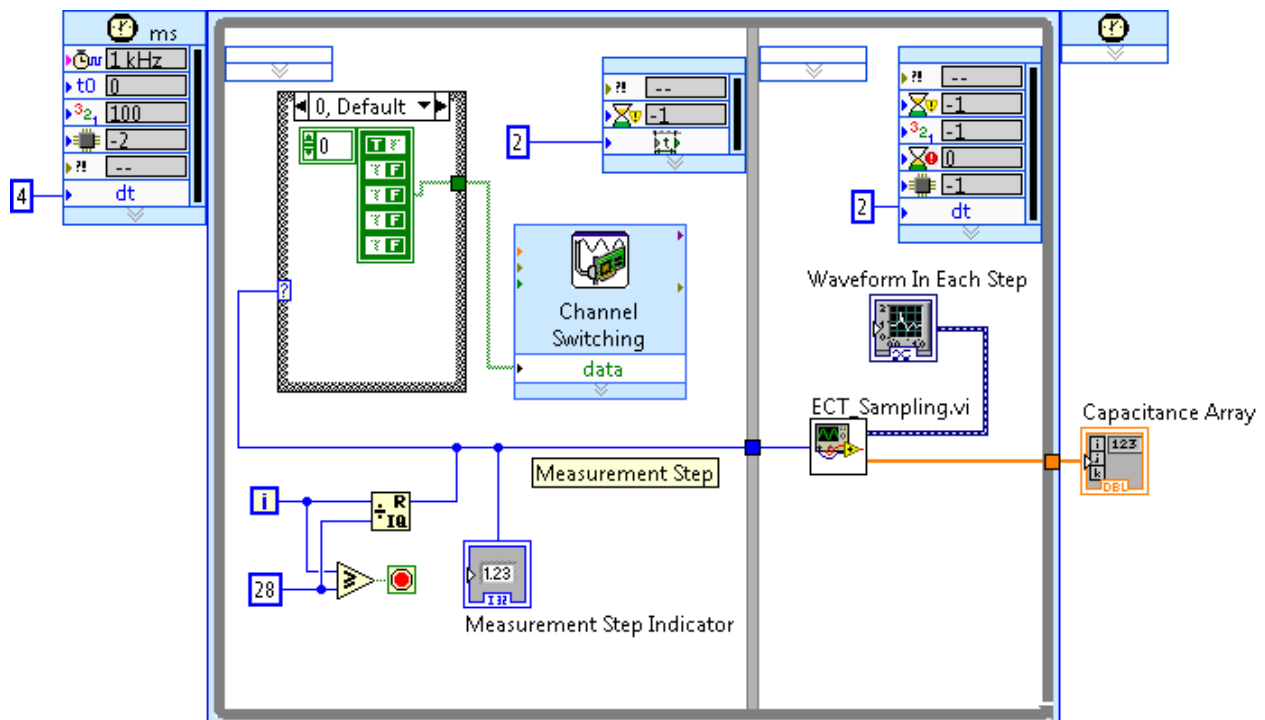


Fig. 3. Design of the Switching Control subVI within a timed loop

## 2.2 Data Sampling (ECT\_Sampling.vi)

The **Data Sampling** subVI runs sequentially after the **Switching Control** subVI to read the voltage  $V_{ij}$  from lock-in amplifier in each measurement step. A detailed view of the subVI design is shown in Figure 4. To reduce the effect of noise from hardware components and DAQ card, the DC voltage  $V_{ij}$  in each measurement step is sampled 50 times at a sampling rate of 512 kSamples/sec. The results are averaged through a *MEAN* subVI. The capacitance value is calculated from  $V_{ij}$  with the known feedback capacitance,  $C_f$  and excitation signal voltage amplitude,  $V_e$ . The relationship is expressed as:

$$C_{ij} = -\frac{V_{ij}}{V_e} C_f \quad (5)$$

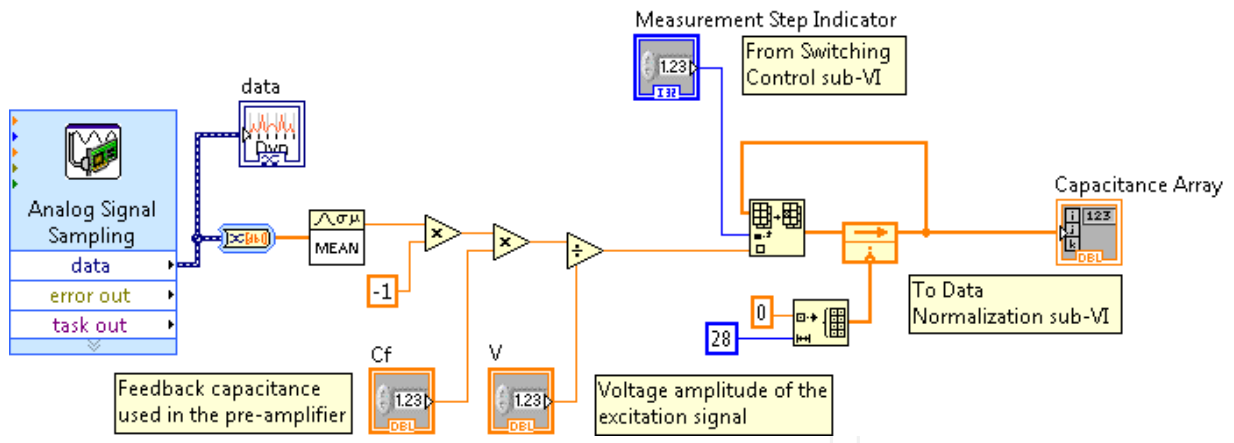


Fig. 4. Design of Data Sampling subVI

A 28x1 capacitance array is created as Table 1 to store all the calculated capacitance values for a scanning frame. As soon as one measurement step finished, the averaged value of  $V_{ij}$  is pushed into the array structure by referring to the *measurement step indicator* imported from **Switching Control** subVI.

### 2.3 Data Normalization

To retrieve the dynamic material distribution within the monitored space, the ECT systems (Isaksen, 1996) remove the effect of background material by normalizing the raw capacitance data with the data measured in two special cases where the ECT sensor is full-filled by the background material, and by the material being monitored. Suppose the corresponding capacitance values measured in these cases are  $\{C_{ij}^b\}$  and  $\{C_{ij}^a\}$ , respectively, the normalized capacitance can be expressed as:

$$\lambda_{ij} = \frac{C_{ij} - C_{ij}^b}{C_{ij}^a - C_{ij}^b} \tag{6}$$

In the VI design, the normalization is realized by the **Data Normalization** subVI as shown in Figure 5. The values of  $\{C_{ij}^b\}$  and  $\{C_{ij}^a\}$  are measured from the preliminary test, e.g. for monitoring the air bubbles in the oil, the **Switching Control** and **Data Sampling** subVI's were run in cases when the pipe is full-filled with oil and air. Corresponding data from the *capacitance array* were copied and pasted into the array modules  $C_a$  and  $C_b$ , respectively, to calculate the normalized capacitance values as expressed in Equation (6).

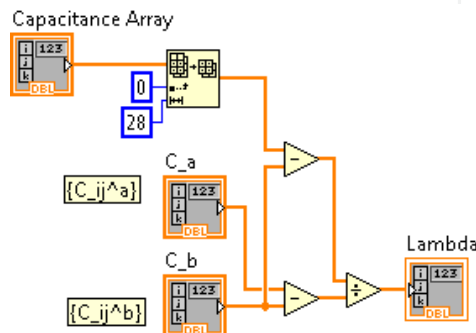


Fig. 5. Design of Data Normalization subVI

## 2.4 Permittivity calculation

Physically, the capacitance values are determined by the permittivity distribution  $\varepsilon(x, y)$ , by following a *forward problem*:  $\lambda_{ij} = f(\varepsilon(x, y))$ . The inverse relationship, called *backward problem*, i.e. estimating the permittivity distribution from the  $N(N-1)/2$  capacitance measurements (Huang et al., 1992), can be expressed as:

$$e(x, y) = f^{-1}(\lambda_{12}, \lambda_{13}, \dots, \lambda_{ij}, \dots, \lambda_{N-1, N}) \quad (7)$$

Unfortunately, it is not always possible to find a closed-form analytical and unique expression for this inverse function (Isaksen, 1996). Therefore, most of the ECT studies (Yang, 2010) apply numerical techniques, which divide the cross section area defined by the electrodes into  $K$  ( $K \in \text{Integer}$ ) pixels, to simplify the boundary conditions and calculations. The permittivity in each of these pixels is assumed to be homogeneous. Thus, the forward problem can be expressed by using the linear matrices:

$$\begin{matrix} \{\lambda_{ij}\} \\ M \times 1 \end{matrix} = S \cdot \begin{matrix} \{\varepsilon_k\} \\ K \times 1 \end{matrix} \quad (8)$$

where  $S$  is an  $M \times K$  Jacobian matrix, also known as the sensitivity matrix, and  $\{\varepsilon_k\}^T$  is a  $K \times 1$  array in which the component  $\varepsilon_k$  is the permittivity of the  $k^{\text{th}}$  ( $1 \leq k \leq K$ ) pixel in the divided sensing area, calculated as:

$$\varepsilon_k = \frac{\varepsilon_k^A - \varepsilon^b}{\varepsilon^a - \varepsilon^b} \quad (9)$$

where  $\varepsilon_k^A$ ,  $\varepsilon^a$ ,  $\varepsilon^b$  are the absolute permittivity of pixel  $k$ , the permittivity of material being detected (e.g. air), and the permittivity of background material (e.g. oil), respectively. The sensitivity map  $S$  contains  $M$  rows. Each row represents the sensitivity distribution within the sensing area when one pair of the electrodes is selected for capacitance measurement. For the 8-electrode ECT,  $M = 28$ , the rows are sorted along the sequence as listed in Table 1. Such a sensitivity matrix can be either experimentally measured (Williams & Beck, 1995) or calculated from a numerical model (Reinecke & Mewes, 1996) by simulating the inter-electrode capacitance values when there is a unit permittivity change in each of the pixels. Due to the limitation of signal-to-noise ratio in the practical capacitance measurement circuitry, the number of electrodes,  $N$ , is generally not greater than 16, to ensure a sufficient surface area for each electrode. Herein, the number of capacitance measurement  $M$  is usually far less than the number of pixels  $K$ . Thus, Equations (8) doesn't have a unique solution.

One of the generally used methods to provide an estimated solution for Equation (8) is Linear Back-Projection (LBP) by which the permittivity of pixel  $k$  is calculated as:

$$\{\hat{\varepsilon}_k\} = \frac{S^T \cdot \{\lambda_{ij}\}}{S^T \cdot u_\lambda} \quad (10)$$

Where  $u_\lambda = [1, 1, \dots, 1]$  is a  $M \times 1$  identity vector.

Practically, the LBP algorithm is realized in the VI design as shown in Figure 6. The vector of normalized capacitance values (*Norm Capacitance*) is imported from the **Data Normalization** subVI. The calculated sensitivity values from a numerical model are pre-loaded in the *constant Sensitivity Matrix* ( $S$ ). The operation of matrix transpose, matrix multiplication, and numerical division in Equation (9) are realized by using the *2D Array Transpose*, *Matrix Multiplication*, and *number division* modules as shown in Figure 6.



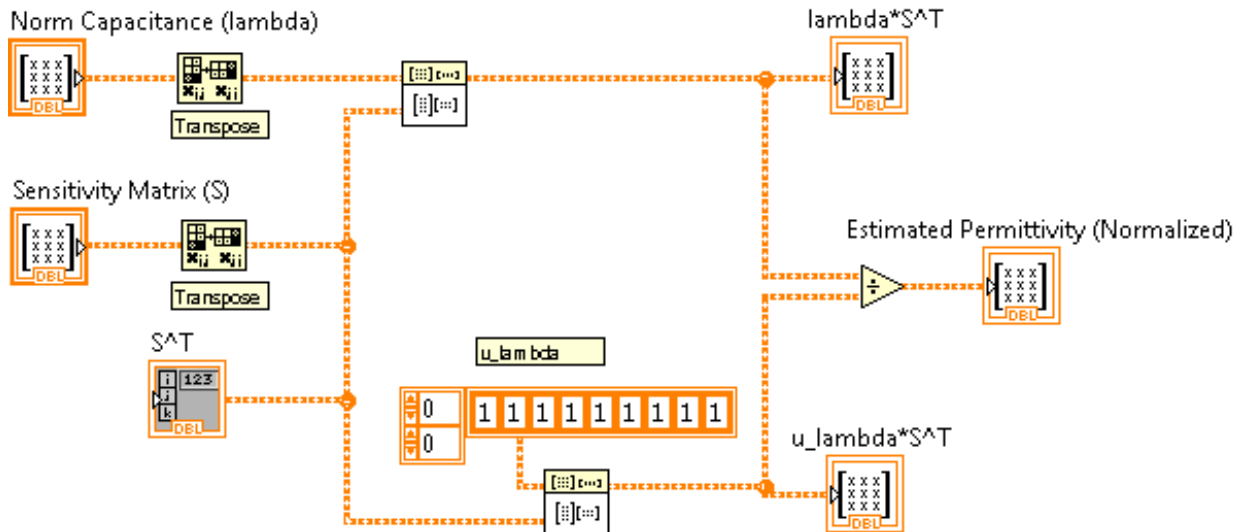


Fig. 6. Permittivity Calculation subVI designed with LBP algorithm

Mathematically, the LBP method uses the transposed sensitivity matrix  $S^T$  as an estimation of the inverse matrix  $S^{-1}$  in calculating the permittivity values. The LBP method can be further expanded by adding the additional subVI's to improve the accuracy in permittivity estimation. One of the optional methods is the Tikhonov Regularization (TR) developed by Tikhonov and Arsenin in 1977 (Tikhonov and Arsenin, 1977). The permittivity calculation using the general TR method can be expressed as:

$$\{\hat{\epsilon}_k\} = \frac{S_{TR}^T \cdot \{\lambda_{ij}\}}{S_{TR}^T \cdot u_\lambda} \quad \text{where} \quad S_{TR}^T = (S^T \cdot S + \mu \cdot I)^{-1} \cdot S^T \cdot \{\lambda_{ij}\} \quad (11)$$

where  $\mu$  is the regularization factor,  $I$  is an  $M \times M$  identity matrix. As compared to Equation (8), the TR method replace the  $S^T$  with the matrix  $(S^T \cdot S + \mu \cdot I)^{-1} \cdot S^T$ . Thus, the TR method can be practically realized by applying a series of operations on the sensitivity matrix  $S$  as shown in Figure 7.

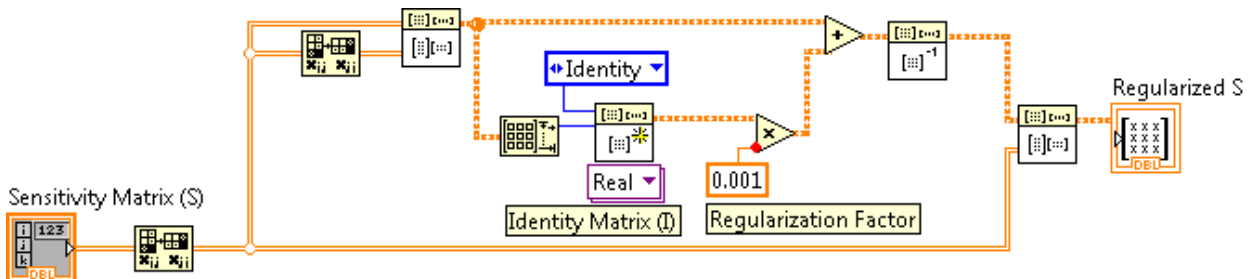


Fig. 7. SubVI design to realize TR for ECT

The accuracy of the TR method depends on the value of regularization factor  $\mu$ . A small value of  $\mu$  will result in a small approximation error but the result will be sensitive to the errors in measurement. In other words, the noise and fluctuation in measured signals produces large artifacts in the generated image when  $\mu$  is small. Conversely, a large value of  $\mu$  produces the image with small artifacts but increases the approximation error. Although some methods (Golub et al., 1979; Hansen, 1992) have been developed to estimate the optimal value of  $\mu$ , they are not widely used due to the unavailability of prior noise

information or the laborious calculation (Yang & Peng, 2003). In most of the applications, the value of  $\mu$  in ECT is chosen empirically in the range from 0.01 to 0.0001. In the example shown in Figure 7, a value of 0.001 is adopted for detecting air bubbles in the oil.

### 2.5 Mesh Generation

When permittivity values are calculated for all the 512 pixels, a map of the meshed sensing area is created by the **Mesh Generation** subVI, as shown in Figure 8. The location and shape of these pixels are pre-written into a TEXT file in the format as shown in Figure 9.

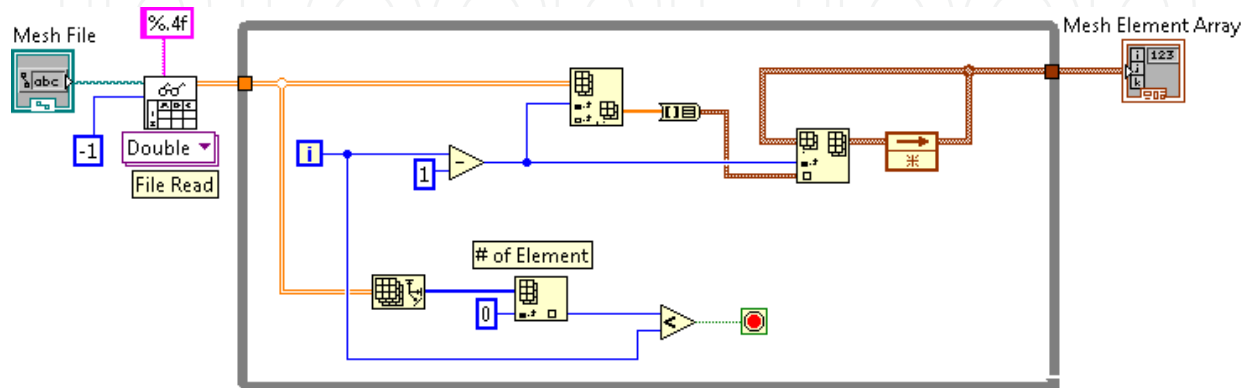


Fig. 8. Design of Mesh Generation subVI

The three columns of the file list  $x$ ,  $y$ , and  $z$  ( $z=0$  for 2-D display) coordinates of all the nodes. Since the sensing area is meshed with four-node pixels, the first four rows in the file represent the nodes included in pixel 1, sorted in counter-clock wise. Consequently the rows 5~8 represent the second pixel and so on. These coordinates are imported into the LabVIEW program by the *File Read* block, and then converted into a 2-dimensional array ( $2 \times 2048$ ), *Mesh Element Array*, which is readable by the **Image Generation** subVI.

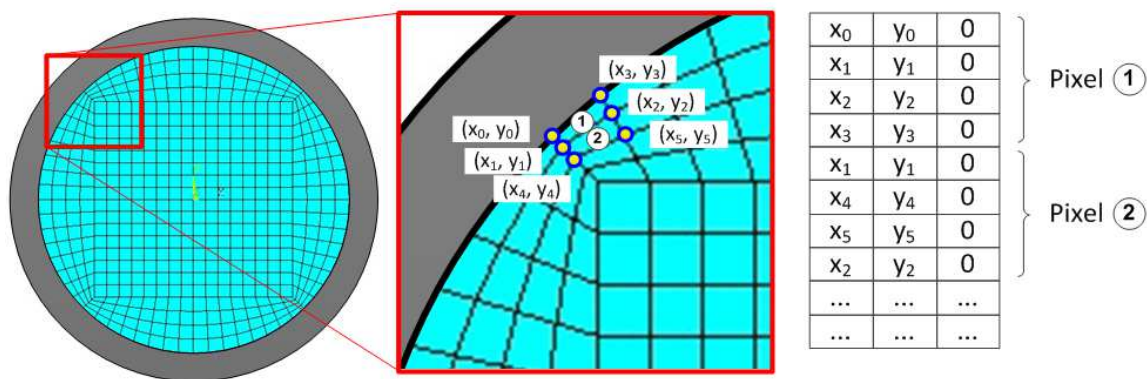


Fig. 9. Designed mesh for the 8-electrode ECT and the format of the Mesh File

### 2.6 Image Generation

Figure 10 shows the block diagram of the designed **Image Generation** subVI where operation functions are built within a loop structure. In each round of the looped operation functions, the **Image Generation** subVI organize the permittivity values measured through **Switching Control**, **Data Sampling**, **Data Normalization**, and **Permittivity Calculation** subVI's, together with the mesh information generated by **Mesh Generation** subVI to create a frame image showing the permittivity distribution within the sensing area.

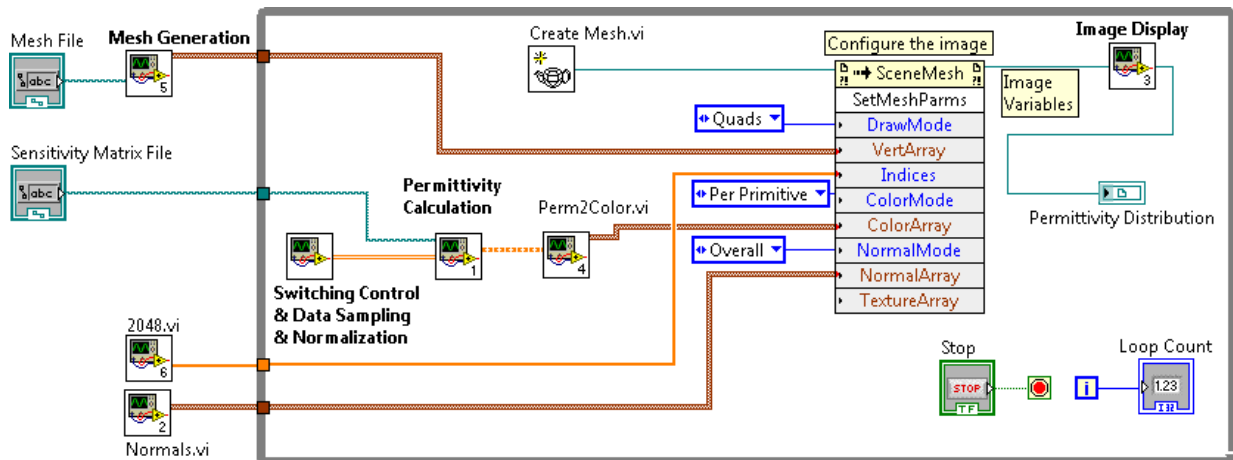


Fig. 10. Design of Image Generation subVI

Four functional subVI's, *Create Mesh.vi*, *2048.vi*, *Normals.vi*, and *Perm2Color.vi* are created in the **Image Generation** subVI to process the permittivity data as well as generate constant parameters for the image:

- The *Create Mesh.vi* generates a Cartesian coordinates array cluster of the node points of the permittivity mesh elements.
- The *2048.vi* produces an array of ordinal numbers, used to identify the order of the elements in the mesh.
- The *Normals.vi* produces the vectors to be normal to the elements in the mesh; this should be uniform to avoid shading discrepancies.
- The *Perm2Color.vi* converts the estimated permittivity values of each pixel,  $\hat{\epsilon}_k$ , (in the range 0~1), to the RGB (Red, Green, Blue, 0~255) color series by following the relationship such that the material of being monitored is displayed in red, while the background material is displayed in blue. To highlight the interface between the two different materials, the permittivity close to mid-point  $0.45 < \hat{\epsilon}_k \leq 0.55$  is displayed in yellow. The corresponding permittivity-to-color conversion can be expressed as:

$$\begin{cases} R_k = 255 \\ G_k = \frac{1 - \hat{\epsilon}_k}{1 - 0.55} \cdot 255 \text{ when } 0.55 < \hat{\epsilon}_k \leq 1 \\ B_k = 0 \end{cases} \quad (12)$$

$$\begin{cases} R_k = \frac{\hat{\epsilon}_k - 0.45}{0.55 - 0.45} \cdot 255 \\ G_k = 255 \\ B_k = \frac{0.55 - \hat{\epsilon}_k}{0.55 - 0.45} \cdot 255 \end{cases} \text{ when } 0.45 < \hat{\epsilon}_k \leq 0.55 \quad (13)$$

$$\begin{cases} R_k = 0 \\ G_k = \frac{\hat{\epsilon}_k}{0.45} \cdot 255 \text{ when } 0 \leq \hat{\epsilon}_k \leq 0.45 \\ B_k = 255 \end{cases} \quad (14)$$

## 2.7 Image Display

The image variables created by the **Image Generation** subVI, including coordinates of the nodes as well as the color set for each pixels, are finally processed by the **Image Display** subVI to show the permittivity distribution on the screen. As shown in Figure 11, a total of 6 *Invoke Nodes* (IN) are employed to combine the image variables into a data flow. The image variables are read via IN1 and IN2 as the drawable attributes in a 3D workspace. The IN3 and IN5 set up a ring in gray color to represent the dimension of the pipe container. The direction and diffuse color of the virtual light source are set by IN4 and IN6. The color map of the permittivity distribution is finally displayed by a Graphic Indicator in the front panel as shown in Figure 12.

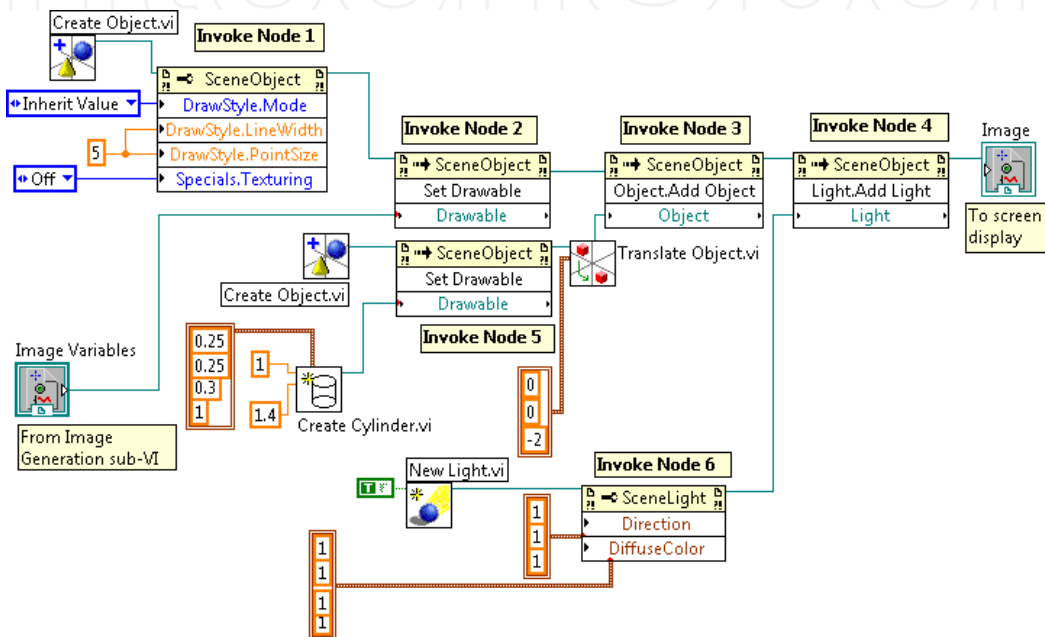


Fig. 11. Design of Image Display subVI

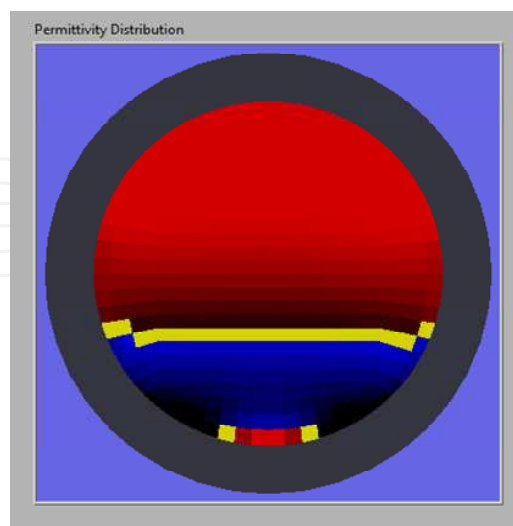


Fig. 12. Front panel of the Image Display subVI

Running on a desktop computer with 3.33GHz Core Duo CPU, the image generation and image display subVI's takes about 10 ms to process each frame of permittivity distribution.

The time delay is measured by looping the subVI's for 1,000 times. Such a time delay needs to be considered in the frame rate calculation as discussed in section 2.2, where the data sampling and circuit switching control take 112 ms per frame. Thus, the total frame rate for the online ECT VI can be calculated as  $1/[(112+10) \cdot 10^{-3}] = 8$  frames/s. It should be noticed that the frame rate is constrained by the timer settings in the general LabVIEW program. In case where higher frame rate is required, the improvement can be realized by employing the Real-time LabVIEW module or applying the multiple/receiving schemes (Fan & Gao, 2011).

### 3. Experiment

The designed VI together is tested with an 8-electrode ECT sensor as shown in Figure 13. The ECT sensor is built on a 40 mm diameter plastic pipe. The eight electrodes are installed on the outer surface of the pipe; each covers  $42^\circ$  along the circumference and 50 mm along the axial direction. At each end of the electrodes, a 10 mm wide circular copper foil is installed as guard-electrodes. During the measurement cycles, the guard-electrodes are electrically grounded to prevent the electric field from spreading axially out of the space determined by the electrodes. The measurement circuit includes the sine wave generation module, switching control logics, pre-amplifiers, and a built-in lock-in amplifier. The output voltage from the lock-in amplifier,  $V_{ij}$ , is sampled and recorded by the desktop computer via an NI PCI6259 DAQ card. Five digital I/O ports PORT0\_Line0 to PORT0\_Line4 are used to send switching control commands to the circuit. An ATMEGA 128L microcontroller is used in the measurement circuit as a decoder module to translate the control commands and initiate the frequency/phase setting of the waveform generators.

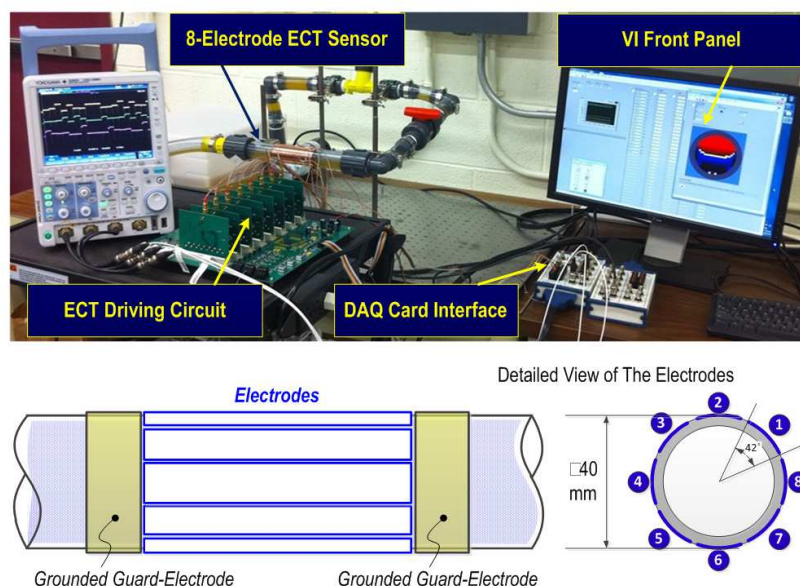


Fig. 13. Experimental setup for ECT

The flexible pipes and connectors in the experimental setup enable setting the ECT electrodes in either horizontal or vertical arrangement to monitor the fluid-gas interface of the oil-air dual phase flow. Figure 14 shows the ECT sensor configured in horizontal arrangement to monitor the oil level. Controlled by an oil pump installed in the pipeline, the oil level is set between 35% and 60% of the pipe inner diameter. It is seen from the five frame images in Figure 14 that the actual oil levels are well represented in the retrieved images generated from the ECT VI.

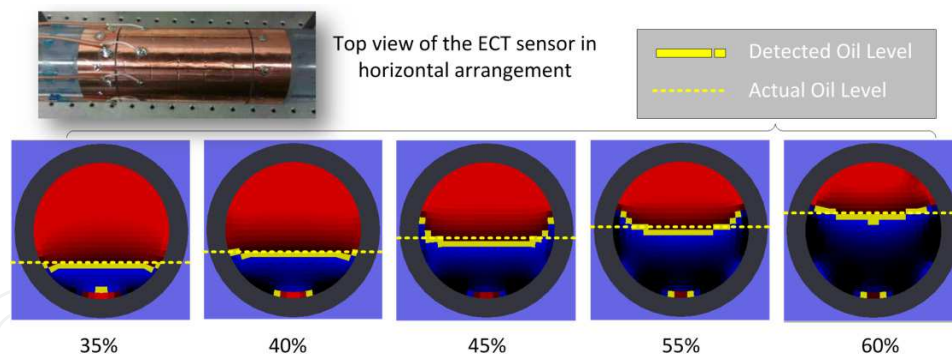


Fig. 14. Oil level monitoring in the horizontal arrangement

Another experiment is conducted to monitor the dynamics of air bubble in the oil in the vertical configuration, as shown in Figure 15. An additional air pump is added into the pipeline to inject air bubbles into the oil flow. Five consecutive frames generated by the ECT VI show the process when a single air bubble travels upward in the oil. Due to the fact that the sensitivity of the ECT sensor reduces at the top and bottom ends of the electrodes, weak signal strength is detected when the bubble enters or leaves the space determined by the electrodes along the axial axis. Variation of the bubble volume in the retrieved images validates such a phenomenon.

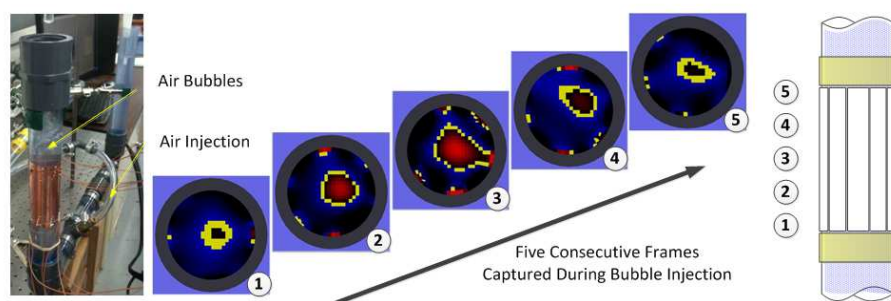


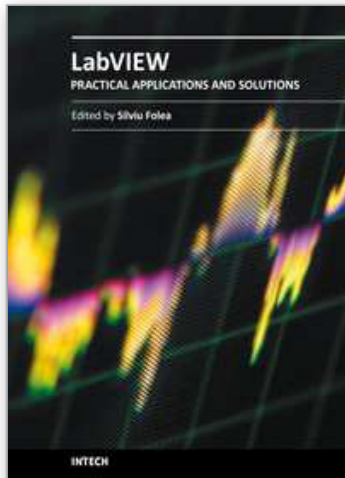
Fig. 15. Air bubble monitoring in the vertical arrangement

#### 4. Conclusion

Electrical capacitance tomography is one of the widely used techniques for monitoring the material distribution within an enclosed container. This chapter introduces the design and realization of a virtual instrument for online ECT sensing. Based on the configuration of hardware circuitry and ECT electrodes, the VI is implemented using seven major functional modules: switching control, data sampling, data normalization, permittivity calculation, mesh generation, image generation, and image display. Each of the functional modules is designed as a subVI to control the measurement circuitry, sample the output signal, and retrieve the permittivity distribution image. Two image retrieving algorithms, Linear Back-Projection and Tikhonov Regularization are implemented in the permittivity calculation subVI. The VI is tested with an 8-electrode ECT sensor built on a 40mm plastic pipe for oil-air flow monitoring. Experimental results have shown that the VI is capable of detecting the oil-air interface as well as catching the dynamics such as the air bubble translation in the oil flow. The introduced VI design can be further expanded to include multiple-excitation (Fan & Gao, 2011), grouping schemes (Olmos, et al., 2008), and advanced image retrieving algorithms to improve the time and spatial resolution of ECT.

## 5. Reference

- Alme, K. J. & Mylvaganam, S. (2007). Comparison of Different Measurement Protocols in Electrical Capacitance Tomography using Simulations", *IEEE Transactions on Instrumentation and Measurement*, Vol.56, No.6, pp.2119–2130.
- Fan, Z. & Gao, R. X. (2011). A New Method for Improving Measurement Efficiency in Electrical Capacitance Tomography," *IEEE Transactions on Instrumentation and Measurement*, Vol.60, No.5, pp.
- Golub, G.; Heath, M. & Wahba, G. (1979). Generalized Cross-Validation as a Method for Choosing a Good Ridge Parameter. *Technometrics*, Vol.21, No.2, pp.215–223.
- Hansen, P. C. (1992). Analysis of Discrete Ill-posed Problems by Means of the L-curve, *SIAM Review*, Vol. 34, No. 3, pp.561–580.
- Huang, S. M. ; Plaskowski, A. ; Xie, C. G. & Beck, M. S. (1989). Tomographic Imaging of Two-component Flow Using Capacitance Sensors. *Journal of Physics E: Scientific Instruments*, Vol.22, No.3, pp. 173-177.
- Huang, S. M.; Xie, C. G.; Thorn, R.; Snowden, D. & Beck, M. S. (1992). Design of sensorelectronics for electrical capacitance tomography," *IEE Proceedings G*, Vol. 139, No.1, pp. 89-98.
- Isaksen, O. (1996). A Review of Reconstruction Techniques for Capacitance Tomography. *Measurement Science and Technology*, Vol.7, No.3, pp. 325–337.
- Marashdeh, Q. & Teixeira, F. L. (2004). Sensitivity Matrix Calculation for Fast 3-D Electrical Capacitance Tomography (ECT) of Flow Systems. *IEEE Transactions on Magnetics*, Vol. 40, No. 2, pp. 1204-1207.
- National Instrumentation.(2001). LabVIEW Real-time User Manual. Available from <http://www.ni.com>.
- Olmos, A. M.; Carvajal, M. A.; Morales, D. P.; García, A. & Palma, A. J. (2008). Development of an Electrical Capacitance Tomography System using Four Rotating Electrodes", *Sensors and Actuators A*, Vol. 128, No.2, pp.366-375.
- Reinecke, N. & Mewes, D. (1996). Recent Developments and Industrial/Research Applications of Capacitance Tomography. *Measurement Science and Technology*, Vol. 7, No.3, pp. 233–246.
- Tikhonov, A. N. & Arsenin, V. Y. (1977). *Solutions of Ill-Posed Problems*. Washington, DC: Winston.
- Warsito, W.; Marashdeh, Q. & Fan, L. S. (2007).Electrical Capacitance Volume Tomography. *IEEE Sensors Journal*, Vol. 7, No. 3, pp. 525-535.
- Williams, R. A. & Beck, M. S. (1995). *Process Tomography: Principles, Techniques and Applications*. Oxford, U.K.: Butterworth-Heinemann.
- Xie, D.; Huang, Z.; Ji, H. & Li, H. (2006). An Online Flow Pattern Identification System for Gas-Oil Two-Phase Flow Using Electrical Capacitance Tomography. *IEEE Transactions on Instrumentation and Measurement*, Vol.55, No.5, pp. 1833 – 1838.
- Yang, W. Q. (1996).Hardware Design of Electrical Capacitance Tomography Systems. *Measurement Science and Technology*, Vol. 7, No.3, pp. 225–232.
- Yang, W. Q & Peng, L. (2003). Image Reconstruction Algorithms for Electrical Capacitance Tomography. *Measurement Science and Technology*, Vol.14. No.1, pp. R1-13.
- Yang, W. Q. (2010). Design of Electrical Capacitance Tomography Sensors," *Measurement Science and Technology*, Vol. 21, No. 4, pp. 1-13.



## **Practical Applications and Solutions Using LabVIEW™ Software**

Edited by Dr. Silviu Folea

ISBN 978-953-307-650-8

Hard cover, 472 pages

**Publisher** InTech

**Published online** 01, August, 2011

**Published in print edition** August, 2011

The book consists of 21 chapters which present interesting applications implemented using the LabVIEW environment, belonging to several distinct fields such as engineering, fault diagnosis, medicine, remote access laboratory, internet communications, chemistry, physics, etc. The virtual instruments designed and implemented in LabVIEW provide the advantages of being more intuitive, of reducing the implementation time and of being portable. The audience for this book includes PhD students, researchers, engineers and professionals who are interested in finding out new tools developed using LabVIEW. Some chapters present interesting ideas and very detailed solutions which offer the immediate possibility of making fast innovations and of generating better products for the market. The effort made by all the scientists who contributed to editing this book was significant and as a result new and viable applications were presented.

### **How to reference**

In order to correctly reference this scholarly work, feel free to copy and paste the following:

Zhaoyan Fan, Robert X. Gao and Jinjiang Wang (2011). Virtual Instrument for Online Electrical Capacitance Tomography, Practical Applications and Solutions Using LabVIEW™ Software, Dr. Silviu Folea (Ed.), ISBN: 978-953-307-650-8, InTech, Available from: <http://www.intechopen.com/books/practical-applications-and-solutions-using-labview-software/virtual-instrument-for-online-electrical-capacitance-tomography>

**INTECH**  
open science | open minds

### **InTech Europe**

University Campus STeP Ri  
Slavka Krautzeka 83/A  
51000 Rijeka, Croatia  
Phone: +385 (51) 770 447  
Fax: +385 (51) 686 166  
[www.intechopen.com](http://www.intechopen.com)

### **InTech China**

Unit 405, Office Block, Hotel Equatorial Shanghai  
No.65, Yan An Road (West), Shanghai, 200040, China  
中国上海市延安西路65号上海国际贵都大饭店办公楼405单元  
Phone: +86-21-62489820  
Fax: +86-21-62489821



© 2011 The Author(s). Licensee IntechOpen. This chapter is distributed under the terms of the [Creative Commons Attribution-NonCommercial-ShareAlike-3.0 License](#), which permits use, distribution and reproduction for non-commercial purposes, provided the original is properly cited and derivative works building on this content are distributed under the same license.

IntechOpen

IntechOpen